This is the peer-reviewed, final accepted version for American Mineralogist, published by the Mineralogical Society of America.
The published version is subject to change. Cite as Authors (Year) Title. American Mineralogist, in press.
DOI: https://doi.org/10.2138/am-2021-7649. http://www.minsocam.org/

**Revision 2**

# Sulfur Content at Sulfide Saturation of Peridotitic Melt at Upper Mantle Conditions

Word count: 4278

Ingrid Blanchard[1#*]; Sumith Abeykoon[1]; Daniel J. Frost[1]; David C. Rubie[1]

[1]Bayerisches Geoinstitut, Universität Bayreuth, 95440 Bayreuth, Germany

[#]Now at Universität Potsdam, Institüt für Geowissenschaft, Karl-Liebknecht-Straße 24/25, 14476 Potsdam

[*]Corresponding author: blanchard@uni-potsdam.de

## 1. Abstract

The concentration of sulfur that can be dissolved in a silicate liquid is of fundamental importance because it is closely associated to several major Earth-related processes. Considerable effort has been made to understand the interplay between the effects of silicate melt composition and its capacity to retain sulfur, but the dependence on pressure and temperature is mostly based on experiments performed at pressures and temperatures below 6 GPa and 2073 K. Here we present a study of the effects of pressure and temperature on sulfur content at sulfide saturation of a peridotitic liquid. We performed 14 multi-anvil experiments using a peridotitic starting composition, and we produced 25 new data at conditions ranging from 7 to 23 GPa and 2173 to 2623 K. We analyzed the recovered samples using both electron microprobe and laser ablation ICP-MS. We compiled our data together with previously published data that were obtained at lower *P-T* conditions and with various silicate melt compositions. We present a new model based on this combined data set that encompasses the entire range of upper mantle pressure-temperature conditions, along with the effect of a wide range of silicate melt compositions. Our findings are

consistent with earlier work based on extrapolation from lower pressure and lower temperature experiments, and show a decrease of the solubility of sulfur at sulfide saturation (SCSS) with increasing pressure and an increase of SCSS with increasing temperature. We have extrapolated our results to pressure- temperature conditions of the Earth's primitive magma ocean, and show that FeS will exsolve from the molten silicate and can effectively be extracted to the core by a process that has been termed the "Hadean Matte". We also discuss briefly the implications of our results for the lunar magma ocean.

**Keywords**: peridotitic melts, sulfur solubility, magma ocean, high pressure, high temperature

## 2. Introduction

Sulfur solubility in silicate melts is important for understanding a number of geological processes such as the formation of magmatic sulfide deposits (Simon and Ripley 2011), volcanic degassing during eruptions (Black et al. 2018), and planetary core-mantle differentiation and late-accretion scenarios (Rubie et al. 2016). The sulfur content at sulfide saturation (SCSS) represents the maximum concentration of sulfur that can be dissolved in a melt at a given pressure and temperature, and as such provides an upper limit to the concentration of sulfur present in melts under reduced conditions. Indeed, at oxygen fugacities below the quartz-fayalite-magnetite buffer, $S^{2-}$ in the silicate replaces $O^{2-}$ in the anion sublattice (Fincham and Richardson 1954). There have been numerous studies of the relation between SCSS and melt composition (e.g., Fincham and Richardson, 1954; Haughton et al., 1974; Holzheid and Grove, 2002; Liu et al., 2007; Mavrogenes and O'Neill, 1999; Fortin et al., 2015; Mysen and Popp, 1980; Smythe et al., 2017). The effects of pressure and temperature have also been studied since the early 1980's. The first study that determined the effects of P and T on SCSS is that of Wendlandt (1982) which

showed that SCSS decreases with increasing pressure and increases with increasing temperature. This study was limited to pressures of ≤ 3 GPa and temperatures up to about 1800 K, but the temperature effect was later confirm by Mavrogenes and O'Neill (1999). Holzheid and Grove (2002) performed an experimental study of the effect of P and T on SCSS up to 2.7 GPa and 1873 K respectively, which verified that SCSS increases with T and decreases with P. Laurenz et al. (2016) performed multi-anvil experiments in order to study the effect of sulfur on the partitioning of highly siderophile elements. They derived a simple relation between SCSS and pressure and temperature that verified the increase of SCSS with T and decrease with P. Recently, Smythe et al. (2017) constructed a model that encompasses a very broad range of compositions for both the sulfide and the silicate phases that could reliably reproduce the value of SCSS for hundreds of natural and experimental data. The vast majority of experimental data used in that study was obtained below 6 GPa and 2073 K, with only three data points above those values for pressure and one for temperature.

The evolution of SCSS at high P and T for peridotitic melt is important for understanding the fate of sulfur in a magma ocean. Indeed, S will exsolve from a magma ocean if its concentration exceeds SCSS. Understanding how the mantle acquired its final concentration of sulfur is still a matter of debate, and has been the subject of several recent studies (e.g. Rose-Weston et al. 2009; Boujibar et al. 2014; Rubie et al. 2016; Suer et al. 2017). The objective of the current study is to extend our knowledge of SCSS of peridotitic melt to high *P-T* conditions. To achieve this, we performed a series of experiments on a silicate melt with a primitive mantle composition that was equilibrated with molten FeS in order to test the effects of high pressure and temperature (up to 23 GPa and 2623 K) on SCSS.

## 3. Experiments and sample analysis

### Experiments

Three sets of experiments were conducted for this study (Table 1). First, in order to determine the effect of pressure on SCSS, we performed eight experiments at a fixed temperature (2473 K) and at pressures that ranged from 7 to 23 GPa. The second and third set of experiments were designed to investigate the effect of temperature on SCSS and consisted of four experiments performed at a fixed pressure of 8 GPa and at temperatures ranging from 2173 to 2473 K and of four experiments at 11 GPa and temperatures ranging from 2273 to 2623 K. As detailed below, most of the experiments were performed using two capsules containing the same starting material, producing a total of 25 new data points. In all cases, synthetic peridotite with a composition of the primitive mantle (Palme and O'Neill, 2014, see composition in Table 2) was used as the starting silicate composition. Silicate powder was prepared from oxides and carbonates and mixed under ethanol in an agate mortar. This mixture was subsequently reduced for 24 h in a 1-atm gas mixing furnace at 1473 K and an $fO_2$ of FMQ-2 (2 log units below the Fayalite-Magnetite–Quartz buffer, O'Neill and Wall 1987). This procedure was repeated twice in order to ensure a fully-reduced starting silicate powder. We used FeS powder as the starting material for the sulfide.

Sulfur saturation experiments were performed in a multi-anvil apparatus using MgO octahedra (doped with $Cr_2O_3$ to enhance thermal insulation) as the pressure medium. Tungsten carbide cubes with 11 mm truncations and 18 mm octahedra (18/11 configuration) were used for experiments at pressures of 7, 8 and 11 GPa in 1000 ton and 5000 ton Kawai-type presses. Experiments at 16, 18 and 21 GPa were carried out using an 18/8 configuration and the experiment at 23 GPa was performed using a 10/4 configuration in a 1000-ton press. All

93 experiments were performed using MgO single crystal capsules, and most were done using two
94 capsules. Stepped LaCrO3-heaters were used for all experiments to minimize the temperature
95 gradient across the sample (Rubie 1999). Temperatures of the experiments were monitored using
96 $W_{97}Re_3$-$W_{75}Re_{25}$ (type D) thermocouples. Based on variations of the temperature-power
97 relationship, temperature uncertainties are estimated to be ±100 K.
98 The starting powders were loaded into single crystal MgO capsules such that a FeS layer was
99 sandwiched between two layers of silicate powder. The molten silicate was equilibrated with
100 molten FeS for 3 to 8 minutes, depending on the temperature (see Table 1). Such durations are
101 sufficient for thermodynamic equilibrium to be achieved given the high temperature of our
102 experiments (Thibault and Walter 1995). After a few minutes at high temperature (see Table 1),
103 experiments were quenched rapidly by switching off the electric power, and then slowly
104 decompressed to room pressure. The recovered samples were cut and polished in preparation for
105 chemical analysis. We present in Fig. 1 an image of a typical recovered sample.
106

107 **Chemical analysis**

108 All recovered samples consist of a sulfide sphere surrounded by quenched silicate melt. Upon
109 quenching, the silicate developed crystals of skeletal olivine, and the sulfide phase displayed a
110 fine-grained quench texture (Fig. 1), which is similar to observations made in previous studies at
111 similar *P-T* conditions (e.g. Mann et al. 2012; Laurenz et al. 2016). As a result of reaction
112 between the MgO capsule and silicate melt, ferropericlase is also present in all samples, and the
113 concentration of MgO in silicate liquid varies in different samples from 36 to almost 53 wt.%. All
114 samples display a finely dispersed sulfide phase along quenched skeletal olivine grain boundaries
115 (Fig. 1b). This texture is a result of quenching from high temperature and the small sulfide blebs

were dissolved in the silicate melt at high temperature and exsolved upon quenching (e.g. Mann et al. 2012; Laurenz et al. 2016).

The recovered samples were carbon coated in order to perform electron microprobe analysis at the Bayerisches Geoinstitut on a JEOL JXA 8200. We used this instrument to determine the concentrations of major elements. We used a defocused beam with a diameter of 10 to 30 microns to analyze the quenched silicate liquid and a defocused beam of 10 or 20 microns in diameter for analyzing the sulfide spheres. We used $FeS_2$, $Cr_2O_3$ and $Fe_2O_3$ as standards for iron and sulfur, chromium and oxygen respectively when analyzing the sulfide phase. Counting times were 20 seconds on the peak and 10 seconds on the background for Fe and S and 60/30 seconds for Cr. We used 15 keV and 20 keV accelerating voltages and 15 nA and 20 nA probe currents when analyzing the silicate and metal respectively. Standards that we used when analyzing the quenched silicate were olivine (for Si, Mg and Fe), $MnTiO_3$ (for Ti), spinel (for Al), andradite (for Ca) and $Cr_2O_3$ (for Cr). Counting times were 20 seconds on peak and 10 seconds on the background for Mg, Si, Al, Fe and Ca, and 30 to 60 seconds for Cr and Ti. For each sample, we performed numerous measurements on various regions of the quenched silicate melt, and averaged the obtained compositions. We report the compositions of all experimental samples in Tables 2 and 3.

Sulfur in the silicate was not measured by electron microprobe but by laser ablation inductively coupled plasma mass spectrometry (LA-ICP-MS), following a procedure described in Laurenz et al. (2016). We used a Coherent COMPexPRO 102 excimer laser (193 nm) attached to a Perkin Elmer ELAN DRC-e quadrupole ICP-MS. Depending on the grain size of the quenched samples and the size of the analyzed zone, we used either a 10 or 5 Hz pulse rate and a spot size of 30 to 70 microns. The sample chamber was flushed with He gas at 0.4 l/min, and an additional 2

ml/min $H_2$ was then admixed on the way to the mass spectrometer to enhance sensitivity. We recorded $^{25}Mg$, $^{27}Al$, $^{29}Si$, $^{32}S$, $^{42}Ca$, $^{49}Ti$, $^{53}Cr$, $^{55}Mn$ and $^{57}Fe$, and used both NIST SRM 610 glass (Jochum et al. 2011) and a basaltic silicate glass standard that contains 5240 ppm S (SB19 from Botcharnikov et al., 2010) as external standards to quantify S in the silicate melt. We analyzed $^{32}S$ because of its high isotopic abundance and $^{16}O^{16}O$ interference is negligible compared to other sources of uncertainty (Rottier and Audétat 2019). Figure 1c shows a close up of one of the samples (Z1640a) on which LA-ICP-MS analyses were performed. As stated above, the fine-grained dispersed metallic grains in the silicate are interpreted to be the result of quench-induced exsolution. They are homogeneously distributed in the silicate phase and anomalous spikes are not visible in most of the laser spectra. In some rare cases, strong, narrow signals appeared in the spectra, as a result of sulfide inclusions ("nuggets") in the silicate (as observed also by Laurenz et al., 2016). In that case, only the signal between the spikes was used to quantify the abundance of S in the silicate melt (Ertel et al. 2006, 2008; Laurenz et al. 2016), hence excluding such inclusions from our measurements.

## Results

In Fig. 2, we show the effects of pressure and temperature on SCSS. From 7 to 23 GPa at a temperature of 2473 K, SCSS drops by almost an order of magnitude (from ~11000 ppm to 1650 ppm). From 2173 to 2473 K at a pressure of 8 GPa, SCSS increases from about 3000 ppm to almost 11000 ppm. Consistent with results obtained over a range of pressures at fixed temperature, SCSS concentrations obtained at 11 GPa are lower than the results obtained at 8 GPa over the whole range of temperatures and also show an increase of SCSS with temperature. Although the starting compositions of all samples were identical, the resulting silicate liquid

compositions varied. The concentration of MgO in the silicate liquid, in particular, varied from approximately 36 wt.% to almost 53 wt.%, the high values relative to that of the starting composition being caused by the reaction of the MgO capsule with the molten silicate. We observe that the MgO content of our samples increases with increasing temperature and decrease with increasing pressure. This is because the concentration of MgO in a melt coexisting with crystalline MgO at a given temperature shifts to a lower MgO content with increasing pressure (Liebske and Frost 2012).

Along with variations in the MgO contents of the recovered samples, we observe variations in other elements such as Si and Fe. The variations in the composition of the quenched silicate liquid is the cause of the scatter in the data plotted in Fig. 2 at a given *P* or *T*. In Fig. 3, we plot the SCSS values for four different samples that were all synthesized at 8 GPa and 2173 K (samples Z1930a and b and Z1983a and b). Figures 3a, b, c illustrate the respective effects of MgO, FeO and $SiO_2$ on SCSS. Increasing the MgO content of the silicate melt results in higher values of SCSS, whereas FeO and $SiO_2$ seem to have the opposite effect. This negative effect of FeO on SCSS is the opposite to that which is usually observe and is linked to the dilution effect of high MgO concentrations as in the experiments presented in Fig. 3: samples containing more MgO have lower FeO concentrations.

The purpose of this study is to investigate the effects of pressure and temperature but, as shown in Fig. 3, it is also mandatory to include compositional effects to fully understand what drives changes of SCSS. In order to model the effects of all these parameters, we describe in the following section the thermodynamic approach that we followed.

## 4. Theoretical considerations

This is the peer-reviewed, final accepted version for American Mineralogist, published by the Mineralogical Society of America.
The published version is subject to change. Cite as Authors (Year) Title. American Mineralogist, in press.
DOI: https://doi.org/10.2138/am-2021-7649. http://www.minsocam.org/

Fincham and Richardson (1954) proposed that at low oxygen fugacities (below the quartz-fayalite-magnetite equilibrium), sulfur dissolves in silicates melts as $S^{2-}$ and by doing so replaces $O^{2-}$ in the anion sublattice. This can be described by the reaction:

$$O^{2-} + \frac{1}{2}S_2 = S^{2-} + \frac{1}{2}O_2 \quad (1)$$

From this reaction, we define $C_S$, the "sulfide capacity" of the melt (Fincham and Richardson 1954), which can be written as:

$$C_S = S_{(\mathrm{ppm})}\left(\frac{fO_2}{fS_2}\right)^{1/2}, \quad (2)$$

with $fO_2$ and $fS_2$ being the oxygen and sulfur fugacities respectively. In addition, the equilibrium between silicate melt and sulfide is described by the reaction:

$$FeO^{\mathrm{silicate}} + \frac{1}{2}S_2 = FeS^{\mathrm{sulfide}} + \frac{1}{2}O_2. \quad (3)$$

The free energy change of equation 3 can be written as:

$$-\frac{\Delta G^0}{RT} = \ln a_{FeS}^{sulfide} - \ln a_{\mathrm{FeO}}^{\mathrm{silicate}} + \ln\left(\frac{fO_2}{fS_2}\right)^{\frac{1}{2}}, \quad (4)$$

where $a_i^j$ is the activity of an element $i$ in a phase $j$ and R is the gas constant. Combining equations 2 and 4, we obtain:

$$\ln S_{(ppm)} = \frac{\Delta G^0}{RT} + \ln C_S + \ln a_{\mathrm{FeS}}^{\mathrm{sulfide}} - \ln a_{\mathrm{FeO}}^{\mathrm{silicate}}, \quad (5)$$

Many studies have proposed that the sulfide capacity is a function of the mole fractions of the oxide compounds on a single cation basis (e.g. Haughton et al. 1974; O'Neill and Mavrogenes 2002; Liu et al. 2007; Ding et al. 2014; Fortin et al. 2015; Namur et al. 2016) such as:

$$\ln C_S = A_0 + \sum_{\mathrm{M}} X_{\mathrm{M}} A_{\mathrm{M}} \quad (6)$$

This is the peer-reviewed, final accepted version for American Mineralogist, published by the Mineralogical Society of America.
The published version is subject to change. Cite as Authors (Year) Title. American Mineralogist, in press.
DOI: https://doi.org/10.2138/am-2021-7649. http://www.minsocam.org/

with $X_M$ being the mole fraction of the respective single oxide component ($SiO_2$, MgO, $AlO_{1.5}$, etc.) and $A_M$ being their related coefficients. Recently, Smythe et al. (2017) used an alternative formalism where the sulfide capacity is also explicitly a function of temperature *T* so that:

$$\ln C_S = A_0 + \sum_M \frac{X_M A_M}{T}. \quad (7)$$

In the following, we test both possibilities, naming the first expression (Eq. 6) as "model 1" and the second expression (Eq. 7) as "model 2".

Equation 5 can then be rewritten as:

$$\ln S_{SCSS} = \frac{\Delta G^0}{RT} + A_0 + \sum_M X_M A_M + \ln a_{FeS}^{sulfide} - \ln a_{FeO}^{silicate} \quad (8)$$

for model 1, and

$$\ln S_{SCSS} = \frac{\Delta G^0}{RT} + A_0 + \sum_M \frac{X_M A_M}{T} + \ln a_{FeS}^{sulfide} - \ln a_{FeO}^{silicate} \quad (9)$$

for model 2.

The term $\Delta G^0$is a function of both pressure (*P*, in GPa) and temperature (*T*, in kelvin), so that:

$$\frac{\Delta G^0}{RT} = -\frac{\Delta S^0}{R} + \frac{\Delta H^0}{RT} + \frac{P\Delta V^0}{RT} = a + \frac{b}{T} + \frac{cP}{T}. \quad (10)$$

Combining equations 8 and 10, we obtain:

$$\ln S_{SCSS} = a' + \frac{b}{T} + \frac{cP}{T} + \sum_M X_M A_M + \ln a_{FeS}^{sulfide} - \ln a_{FeO}^{silicate} \quad (11)$$

for model 1, and by combining equations 9 and 10

$$\ln S_{SCSS} = a' + \frac{b}{T} + \frac{cP}{T} + \sum_M \frac{X_M A_M}{T} + \ln a_{FeS}^{sulfide} - \ln a_{FeO}^{silicate} \quad (12)$$

for model 2. In both cases, 'a'' is the sum of the entropy term of equation 10 and $A_0$ from equations 6 and 7 respectively.

Following Smythe et al. (2017), we assumed that $a_{FeO}^{silicate}$is equal to the mole fraction of FeO in the silicate melt, since the activity coefficient of FeO is close to unity over a wide range of

compositions (Wood and Wade 2013). Nevertheless, we disregarded any experiments from the literature performed at highly reduced conditions (i.e. with less than 0.5 wt.% FeO) because this approximation is not valid at such conditions. We also followed Smythe et al. (2017) in assuming a simple "ideal" solution model where $a_{\mathrm{FeS}}^{\mathrm{sulfide}}$ can be approximated by $X_{\mathrm{FeS}}^{\mathrm{sulfide}}$, as shown by Kiseeva and Wood (2013, 2015). In that case, $X_{\mathrm{FeS}}^{\mathrm{sulfide}}$ is equal to the molar ratio Fe/(Fe+Ni+Cu). We combined our new dataset of 25 results with data from the literature obtained at lower pressures and temperatures, and over a broad range of silicate melt compositions. We used the database provided in Smythe et al. (2017) to which we added two high pressure data points of Laurenz et al. (2016) (Z1311b and H4184b). We selected only those two data points from the Laurenz et al. (2016) study because, in contrast to the other results, the concentrations of highly siderophile elements are low (< 2 wt.%) so that our approximation of ideal solution for FeS is still valid. In total, we used 420 experimental data points.

We performed multivariable linear regressions of the combined data set in order to fit equations 11 and 12 respectively. The results are presented in Table 4 and show very good reproducibility of the data with $R^2$ of 0.91 and 0.92 for models 1 and 2 respectively. In both cases, the derived $A_M$ parameters are all negative, apart from the cross term $A_{SiFe,}$ and are consistent with the results of Smythe et al. (2017) that are presented for comparison in Table 4. The pressure term is very close for both models (-193 $GPa.K^{-1}$ for model 1 and -190 $GPa.K^{-1}$ for model 2). Both models predict higher S solubilities with increasing temperature, but for model 1, we derive a temperature dependence (the b term) that is negative, whereas for model 2, the temperature dependence is positive. This result is similar to that obtained by Smythe et al. (2017), where the positive dependence on temperature in model 2 is accommodated by the $X_M A_M/T$ terms. Both

models resulted in similar predictions of SCSS so, for simplicity, we use the results of model 1 below in the discussion.

In Fig. 4 we compare the predictions of model 1 with the experimental data. The model predictions are in very good agreement with the data that cover a wide range of compositions, as well as pressure-temperature conditions.

## 5. Discussion

The decrease of SCSS with pressure at constant temperature was anticipated from previous studies (*e.g.*, Mavrogenes and O'Neill, 1999; Wendlandt, 1982, Smythe et al., 2017) but this is the first time that it has been demonstrated over a wide pressure range. Figure 5 shows a comparison of our model with the results of previous studies (Mavrogenes and O'Neill 1999; Liu et al. 2007; Fortin et al. 2015; Laurenz et al. 2016; Smythe et al. 2017) along with our experimental data obtained at 2473 K. In this figure, the temperature is fixed at 2473 K and a single silicate melt composition representative of the mean composition of our experimental samples is used for our model and previously published models that include a silicate melt composition dependency. We also assumed that $a_{FeS}$=1. The dependency of SCSS on pressure of our model plots at higher values than all the other models, which were based on lower *P-T* experiments, and a more restricted range of compositions. Our experiments involved silicate melts that are ultramafic with high MgO contents, whereas most previous studies were performed using silicates that contained less than 18 wt.% MgO (Smythe et al., 2017; Mavrogenes et al., 1999; Fortin et al., 2015; Liu et al., 2007). Our MgO-rich compositions are more realistic for understanding mantle processes because the primitive mantle is considered to contain ~ 37 wt.% MgO (Palme and O'Neill, 2014). Laurenz et al. (2016) proposed a model of the dependency of

SCSS on pressure and temperature using high-pressure high-temperature experiments, but they doped most of their samples with high concentrations of chalcophile elements that may influence SCSS by affecting the FeS activity.

Figure 6 shows calculated values of SCSS at different pressures and temperatures, according to equation 11, and using the Primitive Upper Mantle (PUM) composition of Palme and O'Neill (2014) ($SiO_2$ = 45.8 wt.%, MgO = 37.09 wt.%, FeO = 8.17 wt.%, $Al_2O_3$ = 4.53 wt.%, CaO = 3.68 wt.%, $Cr_2O_3$ = 0.37 wt.%, $TiO_2$ = 0.21 wt.%, MnO = 0.14 wt.%, to which we added $H_2O$ = 0.01 wt.%) and for the ideal case of $a_{FeS}$=1. This figure shows the effect of pressure at a given temperature on the calculated value of SCSS, and shows that at low pressure and high temperature, the value of SCSS is high (almost 1.5 wt.%). Conversely, SCSS at high pressure is low and does not change much over the temperature range 2000 to 2500 K, decreasing to about 3000 ppm at 3000 K and 25 GPa.

## 6. Implications

We have demonstrated, in accordance with previous studies, that SCSS is a strong function of both temperature and pressure. Figure 7 shows the dependence of SCSS on depth in a magma ocean based on a Primitive Upper Mantle composition (Palme and O'Neill 2014). One or several magma oceans developed during the accretion of Earth as a result of energy released by giant impacts (Rubie et al., 2015b). Several lines of evidence show that these magma oceans were deep, with basal pressures exceeding 40 GPa and possibly reaching the core-mantle boundary (e.g. Li and Agee 1996; de Vries et al. 2016). Figure 7a illustrates the variation of SCSS along the peridotite melting curve which is defined here as being approximately midway between the

peridotite liquidus and solidus (Rubie et al. 2015a). No difference can be seen between models from Laurenz et al. (2016) and Smythe et al. (2017), but ours plots with slightly higher concentrations at low pressure and temperature before converging at high pressure. Figure 7b shows SCSS along an adiabatic temperature profile for a magma ocean with a basal pressure of 80 GPa (Miller et al. 1991). In that case, our model is closer to the one of Smythe et al. (2017), whereas the model of Laurenz et al. (2016) predicts much higher SCSS values at low *P-T* conditions. Again, the three models converge at high *P-T*, predicting low SCSS values (< 450 ppm).

Geochemically, the exsolution of droplets of liquid FeS from silicate melt in a magma ocean and their segregation to the core (the "Hadean matte" of O'Neill 1991) is of great importance because the process likely strongly depletes the mantle in highly siderophile elements (HSEs) prior to late accretion (Rubie et al., 2016). FeS droplets exsolve as silicate liquid is transported by convection to pressures >40-60 GPa where SCSS is very low. As the magma ocean cools, assuming that it crystallizes from the bottom up so that its depth progressively decreases with time, the magma is able to retain an increasing concentration of FeS because of the increase in SCSS with decreasing pressure. This is illustrated in Fig. 8 which shows the dependence of SCSS on pressure along different mantle temperature gradients : along the liquidus and solidus of peridotite (Fiquet et al. 2010), and along the current mantle geotherm (Katsura et al. 2010).

However, the effect of pressure is strongly countered by an increase in the crystal fraction during magma ocean crystallization – which concentrates S in the melt – so that FeS will still exsolve and segregate at low pressures. However, once the melt fraction decreases to around 30-50%, exsolved FeS liquid becomes trapped in the silicate matrix and is no longer able to segregate (Stevenson 1990; Minarik et al. 1996; Holzheid et al. 2000; Costa et al. 2009; Solomatov 2015).

316 At this point, the process of late accretion starts and establishes most of the current HSE
317 concentrations in the bulk silicate Earth (Rubie et al. 2016).
318
319 Pressures in the lunar mantle are much lower than in Earth's mantle so the mechanism by which
320 FeS and HSE can segregate to the deep lunar mantle and/or the core is quite different (Morbidelli
321 et al. 2018). Because of very high values of SCSS at low pressures (Figs. 6 and 7), FeS only
322 exsolved from the lunar magma ocean during its late stages of crystallization at shallow depths as
323 the residual melt fraction became small. This means that FeS was trapped in the silicate matrix,
324 as described above. However, it is considered that the Moon's mantle crystallized with an
325 inverted density structure that resulted in a major overturn event (Hess and Parmentier 1995;
326 Elkins-Tanton et al. 2011). This overturn, which likely occurred after an extended crystallization
327 history, transported FeS and HSE's to the deep mantle and/or core and is the cause of the low
328 HSE concentrations in the bulk of the lunar mantle today (Morbidelli et al. 2018).
329
330 **Acknowledgments**
331 We acknowledge two anonymous reviewers, the editor and associate editor for their valuable
332 comments and suggestions. We thank members of the mechanical, electronics and polishing
333 workshops at BGI for their invaluable help with preparing the sample assemblies for high
334 pressure experiments and polishing the samples. Detlef Krauße is thanked for his assistance with
335 the electron microprobe, and Andreas Audétat for his precious help with LA-ICP-MS. IB
336 acknowledges funding through German Science Foundation (DFG) Priority Program SPP1833
337 "Building a Habitable Earth" (Ru1323/10-1).
338

## References

Black, B.A., Neely, R.R., Lamarque, J., Elkins-tanton, L.T., Kiehl, J.T., Shields, C.A., Mills, M.J., and Bardeen, C. (2018) Systemic swings in end-Permian climate from Siberian Traps carbon and sulfur outgassing. Nature Geoscience, 11.

Boujibar, A., Andrault, D., Bouhifd, M.A., Bolfan-Casanova, N., Devidal, J.-L., and Trcera, N. (2014) Metal-silicate partitioning of sulphur, new experimental and thermodynamic constraints on planetary accretion. Earth and Planetary Science Letters, 391, 42–54.

Brenan, J.M. (2008) Re-Os fractionation by sulfide melt-silicate melt partitioning: A new spin. Chemical Geology, 248, 140–165.

Costa, A., Caricchi, L., and Bagdassarov, N. (2009) A model for the rheology of particle-bearing suspensions and partially molten rocks. Geochemistry, Geophysics, Geosystems, 10, 1–13.

de Vries, J., Nimmo, F., Melosh, H.J., Jacobson, S.A., Morbidelli, A., and Rubie, D.C. (2016) Impact-induced melting during accretion of the Earth. Progress in Earth and Planetary Science, 3.

Ding, S., Dasgupta, R., and Tsuno, K. (2014) Sulfur concentration of martian basalts at sulfide saturation at high pressures and temperatures - Implications for deep sulfur cycle on Mars. Geochimica et Cosmochimica Acta, 131, 227–246.

Elkins-Tanton, L.T., Burgess, S., and Yin, Q.Z. (2011) The lunar magma ocean: Reconciling the solidification process with lunar petrology and geochronology. Earth and Planetary Science Letters, 304, 326–336.

Ertel, W., Walter, M.J., Drake, M.J., and Sylvester, P.J. (2006) Experimental study of platinum solubility in silicate melt to 14 GPa and 2273 K: Implications for accretion and core formation in Earth. Geochimica et Cosmochimica Acta, 70, 2591–2602.

362 Ertel, W., Dingwell, D.B., and Sylvester, P.J. (2008) Siderophile elements in silicate melts — A
363 review of the mechanically assisted equilibration technique and the nanonugget issue.
364 Chemical Geology, 248, 119–139.
365 Fincham, C.J.B., and Richardson, F.D. (1954) The behaviour of sulphur in silicate and alum inate
366 melts. Proceedings of the Royal Society, 223.
367 Fiquet, G., Auzende, A.L., Siebert, J., Corgne, A., Bureau, H., Ozawa, H., and Garbarino, G.
368 (2010) Melting of peridotite to 140 gigapascals. Science, 329, 1516–1518.
369 Fortin, M., Riddle, J., Desjardins-langlais, Y., and Baker, D.R. (2015) The effect of water on the
370 sulfur concentration at sulfide saturation (SCSS) in natural melts. Geochimica et
371 Cosmochimica Acta, 160, 100–116.
372 Gaetani, G.A., and Grove, T.L. (1997) Partitioning of moderately siderophile elements among
373 olivine, silicate melt, and sulfide melt: Constraints on core formation in the Earth and Mars.
374 Geochimica et Cosmochimica Acta, 61, 1829–1846.
375 Haughton, D.R., Roeder, P.L., and Skinner, B.J. (1974) Solubility of sulfur in mafic magmas.
376 Economic Geology, 69, 451–467.
377 Hess, P.C., and Parmentier, E.M. (1995) A model for the thermal and chemical evolution of the
378 Moon's interior: implications for the onset of mare volcanism. Earth and Planetary Science
379 Letters, 134, 501–514.
380 Holzheid, A., and Grove, T.L. (2002) Sulfur saturation limits in silicate melts and their
381 implications for core formation scenarios for terrestrial planets. American Mineralogist, 87,
382 227–237.
383 Holzheid, A., and Lodders, K. (2001) Solubility of copper in silicate as funcdtion of oxygen and
384 sulfur fugacities teperatures, and silicate composition. Geochimica et Cosmochimica Acta,

65, 1933–1951.

Holzheid, A., Schmitz, M.D., and Grove, T.L. (2000) Textural equilibria of iron sulfide liquids in partly molten silicate aggregates and their relevance to core formation scenarios. Journal of Geophysical Research: Solid Earth, 105, 13555–13567.

Jochum, K.P., Weis, U., Stoll, B., Kuzmin, D., Yang, Q., Raczek, I., Jacob, D.E., Stracke, A., Birbaum, K., Frick, D.A., and others (2011) Determination of reference values for NIST SRM 610-617 glasses following ISO guidelines. Geostandards and Geoanalytical Research, 35, 397–429.

Jugo, P.J., Luth, R.W., and Richards, J.P. (2005) An Experimental Study of the Sulfur Content in Basaltic Melts Saturated with Immiscible Sulfide or Sulfate Liquids at 1300 C and 1 GPa. Journal of Petrology, 46, 783–798.

Katsura, T., Yoneda, A., Yamazaki, D., Yoshino, T., Ito, E., Suetsugu, D., Bina, C., Inoue, T., Wiens, D., and Jellinek, M. (2010) Adiabatic temperature profile in the mantle. Physics of the Earth and Planetary Interiors, 183, 212–218.

Kiseeva, E.S., and Wood, B.J. (2013) A simple model for chalcophile element partitioning between sulphide and silicate liquids with geochemical applications. Earth and Planetary Science Letters, 383, 68–81.

Kiseeva, E.S., and Wood, B.J. (2015) The effects of composition and temperature on chalcophile and lithophile element partitioning into magmatic sulphides. Earth and Planetary Science Letters, 424, 280–294.

Laurenz, V., Rubie, D.C., Frost, D.J., and Vogel, A.K. (2016) The importance of sulfur for the behavior of highly-siderophile elements during Earth's differentiation. Geochimica et Cosmochimica Acta, 194, 123–138.

Li, J., and Agee, C.B. (1996) Geochemistry of mantle-core differentiation at high pressure. Nature, 381, 686–689.

Liebske, C., and Frost, D.J. (2012) Melting phase relations in the MgO-MgSiO 3 system between 16 and 26GPa: Implications for melting in Earth's deep interior. Earth and Planetary Science Letters, 345–348, 159–170.

Liu, Y., Samaha, N., and Baker, D.R. (2007) Sulfur concentration at sulfide saturation (SCSS) in magmatic silicate melts. Geochimica et Cosmochimica Acta, 71, 1783–1799.

Mann, U., Frost, D.J., Rubie, D.C., Becker, H., and Audétat, A. (2012) Partitioning of Ru, Rh, Pd, Re, Ir and Pt between liquid metal and silicate at high pressures and high temperatures - Implications for the origin of highly siderophile element concentrations in the Earth's mantle. Geochimica et Cosmochimica Acta, 84, 593–613.

Mavrogenes, J.A., and O'Neill, H.S.C. (1999) The relative effects of pressure, temperature and oxygen fugacity on the solubility of sulfide in mafic magmas. Geochimica et Cosmochimica Acta, 63, 1173–1180.

Miller, G.H., Stolper, E.M., and Ahrens, T.J. (1991) The equation of state of a molten komatiite 2. Application to komatiite petrogenesis and the Hadean mantle. Journal of Geophysical Research, 96, 849–864.

Minarik, W.G., Ryerson, F.J., and Watson, E.B. (1996) Textural entrapment of core-forming melts. Science, 272, 530–533.

Morbidelli, A., Nesvorny, D., Laurenz, V., Marchi, S., Rubie, D.C., Elkins-Tanton, L., Wieczorek, M., and Jacobson, S. (2018) The timeline of the lunar bombardment: Revisited. Icarus, 305, 262–276.

Mysen, B.O., and Popp, R.K. (1980) Solubility of sulfur in CaMgSi2O6 and NaAlSi3O 8 melts at

high pressure and temperature with controlled fO2 and fS2. American Mineralogist, 280, 78–92.

Namur, O., Charlier, B., Holtz, F., Cartier, C., and McCammon, C. (2016) Sulfur solubility in reduced mafic silicate melts: Implications for the speciation and distribution of sulfur on Mercury. Earth and Planetary Science Letters, 448, 102–114.

O'Neill, H.S.C. (1991) The origin of the Moon and the early history of the Earth—A chemical model. Part 2: The Earth. Geochimica et Cosmochimica Acta, 55, 1159–1172.

O'Neill, H.S.C., and Eggins, S.M. (2002) The effect of melt composition on trace element partitioning: an experimental investigation of the activity coefficients of FeO, NiO, CoO, MoO2 and MoO3 in silicate melts. Chemical Geology, 24, 1411–1416.

O'Neill, H.S.C., and Mavrogenes, J.A. (2002) The Sulfide Capacity and the Sulfur Content at Sulfide Saturation of Silicate Melts at 1400 ° C and 1 bar. Journal of Petrology, 43, 1049–1087.

O'Neill, H.S.C., and Wall, V.J. (1987) The Olivine-Orthopyroxene-Spinel Oxygen Geobarometer, the Nickel Precipitation Curve, and the Oxygen Fugacity of the Earth's Upper Mantle. Journal of Petrology, 28, 1169–1191.

Palme, H., and O'Neill, H.S.C. (2014) Cosmochemical Estimates of Mantle Composition. In Treatise on Geochemistry 2nd Edition pp. 1–39. Elsevier Ltd.

Peach, C.L., Mathez, E.A., and Keays, R.R. (1990) Sulfide melt-silicate melt distribution coefficients for noble metals and other chalcophile elements as deduced from MORB : Implications for partial melting. Geochimica et Cosmochimica Acta, 54.

Ripley, E.M., Brophy, J.G., and Li, C. (2002) Copper solubility in a basaltic melt and sulfide liquid/silicate melt partition coefficients of Cu and Fe. Geochimica et Cosmochimica Acta,

66, 2791–2800.

Rose-Weston, L., Brenan, J.M., Fei, Y., Secco, R.A., and Frost, D.J. (2009) Effect of pressure, temperature, and oxygen fugacity on the metal-silicate partitioning of Te, Se, and S: Implications for earth differentiation. Geochimica et Cosmochimica Acta, 73, 4598–4615.

Rottier, B., and Audétat, A. (2019) In-situ quantification of chlorine and sulfur in glasses, minerals and melt inclusions by LA-ICP-MS. Chemical Geology, 504, 1–13.

Rubie, D.C. (1999) Phase Transitions : A Characterising the sample environment in multianvil high-pressure experiments. Phase Transitions : A multinational Journal, 68, 431–451.

Rubie, D.C., Jacobson, S.A., Morbidelli, A., O'Brien, D.P., Young, E.D., de Vries, J., Nimmo, F., Palme, H., and Frost, D.J. (2015a) Accretion and differentiation of the terrestrial planets with implications for the compositions of early-formed Solar System bodies and accretion of water. Icarus, 248, 89–108.

Rubie, D.C., Nimmo, F., and Melosh, H.J. (2015b) Formation of the Earth's Core. In Gerald Schubert (editor-in-chief) Treatise on Geophysics Vol. 9: Evolution of the Earth, 2nd edition pp. 43–79. Elsevier B.V.

Rubie, D.C., Laurenz, V., Jacobson, S.A., Morbidelli, A., Palme, H., Vogel, A.K., and Frost, D.J. (2016) Highly siderophile elements were stripped from Earth's mantle by iron sulfide segregation. Science, 353, 1141–1144.

Simon, A.C., and Ripley, E.M. (2011) The Role of Magmatic Sulfur in the Formation of Ore Deposits. Reviews in Mineralogy and Geochemistry, 73, 513–578.

Smythe, D.J., Wood, B.J., and Kiseeva, E.S. (2017) The S content of silicate melts at sulfide saturation: New experiments and a model incorporating the effects of sulfide composition. American Mineralogist, 102, 795–803.

Solomatov, V. (2015) Magma Oceans and Primordial Mantle Differentiation, 81–104 p. Treatise on Geophysics: Second Edition Vol. 9. Elsevier B.V.

Stevenson, D.J. (1990) Fluid dynamics of core formation. Origin of the Earth, 1, 231–249.

Suer, T.A., Siebert, J., Remusat, L., Menguy, N., and Fiquet, G. (2017) A sulfur-poor terrestrial core inferred from metal–silicate partitioning experiments. Earth and Planetary Science Letters, 469, 84–97.

Thibault, Y., and Walter, M.J. (1995) The influence of pressure and temperature on the metal-silicate partition coefficients of nickel and cobalt in a model Cl chondrite and implications for metal segregation in a deep magma ocean. Geochimica et Cosmochimica Acta, 59, 991–1002.

Wendlandt, R.F. (1982) Sulfide saturation of basalt and andesite melts at high pressures and temperatures. American Mineralogist, 67, 877–885.

Wohlers, A., and Wood, B.J. (2015) A Mercury-like component of early Earth yields uranium in the core and high mantle 142 Nd. Nature.

Wood, B.J., and Kiseeva, E.S. (2015) Trace element partitioning into sulfide: How lithophile elements become chalcophile and vice versa. American Mineralogist, 100, 2371–2379.

Wood, B.J., and Wade, J. (2013) Activities and volatilities of trace components in silicate melts: A novel use of metal-silicate partitioning data. Contributions to Mineralogy and Petrology, 166, 911–921.

Figure 1: a) Backscattered electron image of sample Z1640b obtained at 11 GPa and 2373 K using a multi-anvil apparatus. b) Close up of typical quenched silicate liquid on which electron microprobe analysis was performed. c) Close up of quenched silicate liquid on which LA-ICP-MS analysis was performed.

Figure 2: Experimental results showing the effects of pressure and temperature on SCSS. (a) Data obtained at a fixed temperature of 2473 K are plotted as a function of pressure. (b) Data obtained at fixed pressures of 8 GPa (circles) and 11 GPa (stars) are plotted as a function of temperature.

Figure 3: Comparison of the effects of MgO, FeO and $SiO_2$ concentrations in the silicate melt on SCSS at a fixed pressure and temperature (8 GPa and 2173 K) in samples Z1930a, Z1930b, Z1983a and Z1983b.

Figure 4: Comparison of model 1 (equation 11) with our high P-T experimental data (red circles) and data from the literature (unfilled black circles). References: Wendlandt 1982; Peach et al. (1990); Gaetani and Grove (1997); Holzheid and Lodders (2001); O'Neill and Mavrogenes (2002); Ripley et al. (2002); Holzheid and Grove (2002); Jugo et al. (2005); Liu et al. (2007); Brenan (2008); Kiseeva and Wood (2013, 2015); Ding et al. (2014); Wohlers and Wood (2015); Wood and Kiseeva (2015); Fortin et al. (2015); Laurenz et al. (2016); Smythe et al. (2017).

Figure 5: Comparison of our model of the dependency of SCSS on pressure (bold line, equation 11) at 2473 K with the predictions of previously published models. For models that are composition-dependent (this study, Fortin et al., 2015; Liu et al., 2007; Smythe et al., 2017), we used the equations proposed in the respective publications using the mean composition of the silicate melt in our samples: $SiO_2$=40.32 wt.%; MgO=46.27 wt.%; FeO=6.19 wt.%; $Al_2O_3$ = 2.98 wt.%; CaO = 3.14 wt.%; $Cr_2O_3$ = 0.11 wt.%; $TiO_2$ = 0.14 wt.%; MnO = 0.06 wt.%; $H_2O$ = 0.01 wt.%. In all cases the temperature is 2473 K and $a_{FeS}$=1 is assumed.

Figure 6: Dependency of SCSS on pressure and temperature based on the fit of equation 11. The composition of the silicate is the primitive upper mantle composition proposed by Palme and O'Neill (2014) ($SiO_2$ = 45.8 wt.%, MgO = 37.09 wt.%, FeO = 8.17 wt.%, $Al_2O_3$ = 4.53 wt.%, CaO = 3.68 wt.%, $Cr_2O_3$ = 0.37 wt.%, $TiO_2$ = 0.21 wt.%, MnO = 0.14 wt.%) to which we added $H_2O$ = 0.01 wt.%.

Figure 7: Evolution of SCSS with pressure in a silicate melt of Primitive Upper Mantle composition (Palme and O'Neill 2014) along peridotite melting curve (a) and along 80 GPa magma ocean adiabat (b, Miller et al. 1991).

Figure 8: SCSS as a function of pressure along different mantle temperature profiles for the primitive upper mantle composition of Palme and O'Neill (2014).

538 **Tables**

539 **Table 1:** Experimental conditions of our experiments.

540

| Runs | P (GPa) | T (K) | Assembly | Duration (min) |
|---|---|---|---|---|
| Z1896a | 16 | 2473 | 18/11 | 5 |
| Z1896b | 16 | 2473 | 18/11 | 5 |
| Z1913a | 18 | 2473 | 18/11 | 5 |
| Z1913b | 18 | 2473 | 18/11 | 5 |
| Z1914a | 21 | 2473 | 18/8 | 5 |
| Z1914b | 21 | 2473 | 18/8 | 5 |
| H4879a | 11 | 2473 | 18/11 | 5 |
| H4879b | 11 | 2473 | 18/11 | 5 |
| H4894 | 23 | 2473 | 10/4 | 5 |
| Z1930a | 8 | 2173 | 18/11 | 3 |
| Z1930b | 8 | 2173 | 18/11 | 3 |
| Z1983a | 8 | 2173 | 18/11 | 5 |
| Z1983b | 8 | 2173 | 18/11 | 5 |
| Z1987a | 8 | 2473 | 18/11 | 3 |
| Z1987b | 8 | 2473 | 18/11 | 3 |
| Z1996a | 8 | 2273 | 18/11 | 5 |
| Z1996b | 8 | 2273 | 18/11 | 5 |
| Z1640b | 11 | 2373 | 18/11 | 5 |

| | | | | |
|---|---|---|---|---|
| Z1641a | 11 | 2273 | 18/11 | 5 |
| Z1641b | 11 | 2273 | 18/11 | 5 |
| H4486a | 11 | 2473 | 18/11 | 5 |
| H4486b | 11 | 2473 | 18/11 | 5 |
| Z1644a | 7 | 2473 | 18/11 | 5 |
| Z1651a | 11 | 2623 | 18/11 | 5 |
| Z1651b | 11 | 2623 | 18/11 | 5 |

541

542 **Table 2:** Composition of the quenched silicate liquid obtained by EPMA (in wt.%) and LA-ICP-MS measurements (in ppm in the case of S, as
543 indicated by *). *N* denotes the number of analyses perform by EPMA and *N** the number of LA-ICP-MS analyses for each sample.

544

| run | P (GPa) | T (K) | *N* | *N** | $SiO_2$ | std | MgO | std | $Al_2O_3$ | std | S* | std | $Cr_2O_3$ | std | CaO | std | FeO | std | $TiO_2$ | std | Total | std |
|---|---|---|---|---|---|---|---|---|---|---|---|---|---|---|---|---|---|---|---|---|---|---|
| Starting material | - | 1473 | - | - | 45.80 | - | 37.09 | - | 4.53 | - | - | - | 0.37 | - | 3.68 | - | 8.17 | - | 0.21 | - | 99.86 | - |
| Z1896a | 16 | 2473 | 24 | 5 | 42.43 | 0.70 | 44.95 | 3.69 | 3.17 | 1.16 | 3602 | 129 | 0.07 | 0.02 | 3.55 | 1.26 | 4.96 | 0.81 | 0.17 | 0.07 | 99.71 | 0.46 |
| Z1896b | 16 | 2473 | 25 | 4 | 42.95 | 0.74 | 45.47 | 1.71 | 2.91 | 0.52 | 6244 | 243 | 0.06 | 0.01 | 3.22 | 0.61 | 3.70 | 0.51 | 0.14 | 0.04 | 99.20 | 0.49 |
| Z1913a | 18 | 2473 | 19 | 5 | 42.08 | 0.57 | 45.81 | 2.27 | 2.84 | 0.73 | 3782 | 174 | 0.09 | 0.02 | 2.94 | 0.74 | 4.94 | 0.54 | 0.14 | 0.05 | 99.31 | 0.57 |
| Z1913b | 18 | 2473 | 18 | 5 | 43.38 | 1.12 | 42.79 | 3.34 | 3.21 | 0.99 | 3908 | 362 | 0.11 | 0.03 | 3.49 | 1.14 | 5.25 | 1.10 | 0.17 | 0.07 | 99.03 | 0.41 |
| Z1914a | 21 | 2473 | 8 | 5 | 42.71 | 1.28 | 44.76 | 2.50 | 3.03 | 0.31 | 4293 | 66 | 0.09 | 0.01 | 3.30 | 1.23 | 4.71 | 0.50 | 0.16 | 0.11 | 99.31 | 0.48 |
| Z1914b | 21 | 2473 | 6 | 5 | 44.46 | 2.34 | 43.48 | 2.07 | 2.09 | 0.52 | 2829 | 139 | 0.06 | 0.01 | 1.82 | 0.93 | 4.91 | 1.19 | 0.06 | 0.05 | 97.15 | 0.45 |
| H4879a | 11 | 2473 | 10 | 4 | 39.08 | 1.02 | 48.36 | 3.23 | 1.82 | 1.05 | 7595 | 392 | 0.08 | 0.02 | 3.69 | 1.79 | 4.52 | 0.94 | 0.07 | 0.04 | 98.82 | 1.01 |
| H4879b | 11 | 2473 | 15 | 6 | 39.17 | 3.31 | 48.85 | 6.51 | 2.78 | 2.22 | 6077 | 241 | 0.09 | 0.05 | 2.94 | 2.27 | 4.82 | 0.98 | 0.09 | 0.05 | 99.36 | 0.48 |
| H4894 | 23 | 2473 | 22 | 5 | 49.31 | 5.02 | 36.05 | 5.64 | 5.18 | 0.66 | 1646 | 273 | 0.36 | 0.03 | 3.70 | 0.71 | 4.68 | 1.15 | 0.13 | 0.04 | 99.47 | 0.80 |
| Z1930a | 8 | 2173 | 11 | 4 | 38.52 | 1.76 | 45.36 | 3.74 | 4.30 | 3.12 | 4626 | 751 | 0.30 | 0.18 | 2.74 | 1.81 | 8.22 | 1.87 | 0.16 | 0.11 | 99.94 | 0.95 |

This is the peer-reviewed, final accepted version for American Mineralogist, published by the Mineralogical Society of America.
The published version is subject to change. Cite as Authors (Year) Title. American Mineralogist, in press.
DOI: https://doi.org/10.2138/am-2021-7649. http://www.minsocam.org/

| | | | | | | | | | | | | | | | | | | | | | | |
|---|---|---|---|---|---|---|---|---|---|---|---|---|---|---|---|---|---|---|---|---|---|---|
| Z1930b | 8 | 2173 | 14 | 5 | 42.47 | 1.04 | 40.48 | 6.17 | 4.05 | 2.14 | 3483 | 533 | 0.29 | 0.08 | 3.67 | 2.02 | 8.24 | 1.14 | 0.20 | 0.17 | 99.78 | 0.71 |
| Z1983a | 8 | 2173 | 11 | 5 | 37.95 | 2.00 | 46.65 | 5.24 | 4.17 | 2.85 | 5589 | 440 | 0.18 | 0.07 | 3.92 | 2.43 | 6.69 | 2.07 | 0.23 | 0.17 | 100.00 | 0.75 |
| Z1983b | 8 | 2173 | 8 | 5 | 38.37 | 1.47 | 49.09 | 2.61 | 1.77 | 0.91 | 5945 | 174 | 0.07 | 0.01 | 3.04 | 1.15 | 6.08 | 1.89 | 0.16 | 0.08 | 99.25 | 0.64 |
| Z1987a | 8 | 2473 | 12 | 4 | 38.19 | 1.11 | 52.97 | 1.59 | 0.92 | 0.58 | 10839 | 898 | 0.06 | 0.03 | 1.03 | 0.63 | 5.62 | 1.17 | 0.04 | 0.02 | 100.06 | 0.70 |
| Z1987b | 8 | 2473 | 17 | 5 | 38.28 | 1.82 | 52.80 | 1.00 | 1.46 | 1.53 | 10187 | 756 | 0.05 | 0.03 | 1.35 | 0.98 | 5.09 | 1.05 | 0.06 | 0.04 | 100.15 | 0.77 |
| Z1996a | 8 | 2273 | 13 | 4 | 36.78 | 3.97 | 52.11 | 3.80 | 2.73 | 1.28 | 8913 | 222 | 0.10 | 0.06 | 2.53 | 1.08 | 5.82 | 1.29 | 0.14 | 0.06 | 101.02 | 1.05 |
| Z1996b | 8 | 2273 | 18 | 5 | 37.82 | 1.37 | 48.79 | 2.89 | 3.08 | 1.38 | 7566 | 209 | 0.08 | 0.06 | 3.45 | 1.71 | 7.48 | 1.45 | 0.15 | 0.07 | 101.65 | 1.64 |
| Z1640b | 11 | 2373 | 45 | 2 | 40.21 | 0.90 | 45.46 | 2.86 | 3.08 | 1.01 | 2963 | 26 | 0.13 | 0.04 | 2.82 | 1.11 | 7.37 | 0.70 | 0.12 | 0.05 | 99.48 | 0.43 |
| Z1641a | 11 | 2273 | 45 | 4 | 39.61 | 0.36 | 41.29 | 0.79 | 4.29 | 0.17 | 3611 | 38 | 0.16 | 0.01 | 5.00 | 0.42 | 9.13 | 0.42 | 0.24 | 0.03 | 100.08 | 0.21 |
| Z1641b | 11 | 2273 | 45 | 2 | 40.12 | 0.08 | 41.55 | 1.07 | 4.34 | 0.38 | 3505 | 81 | 0.17 | 0.02 | 4.86 | 0.44 | 8.27 | 0.23 | 0.23 | 0.03 | 99.88 | 0.32 |
| H4486a | 11 | 2473 | 47 | 3 | 40.54 | 0.26 | 44.83 | 1.41 | 3.21 | 0.55 | 4897 | 141 | 0.01 | 0.00 | 3.67 | 0.66 | 7.29 | 0.26 | 0.18 | 0.02 | 100.20 | 0.22 |
| H4486b | 11 | 2473 | 36 | 2 | 41.12 | 0.29 | 45.61 | 1.15 | 2.95 | 0.66 | 6417 | 233 | 0.10 | 0.02 | 3.26 | 0.53 | 6.67 | 0.46 | 0.15 | 0.02 | 100.49 | 0.31 |
| Z1644a | 7 | 2473 | 47 | 4 | 36.80 | 0.76 | 49.37 | 0.72 | 2.34 | 0.44 | 9019 | 203 | 0.01 | 0.00 | 2.81 | 0.55 | 7.78 | 0.57 | 0.14 | 0.02 | 100.15 | 0.27 |
| Z1651a | 11 | 2623 | 50 | 4 | 38.48 | 0.67 | 49.83 | 1.38 | 2.25 | 0.41 | 7089 | 249 | 0.01 | 0.00 | 2.85 | 0.73 | 6.13 | 0.48 | 0.15 | 0.04 | 100.40 | 0.32 |
| Z1651b | 11 | 2623 | 50 | 4 | 37.21 | 1.35 | 49.95 | 1.81 | 2.54 | 0.22 | 6424 | 465 | 0.10 | 0.01 | 2.94 | 0.73 | 6.38 | 0.37 | 0.14 | 0.04 | 99.91 | 0.21 |

545

546

This is the peer-reviewed, final accepted version for American Mineralogist, published by the Mineralogical Society of America.
The published version is subject to change. Cite as Authors (Year) Title. American Mineralogist, in press.
DOI: https://doi.org/10.2138/am-2021-7649. http://www.minsocam.org/

547 **Table 3:** Compositions of the sulfide phase measured with EPMA (in wt. %). The sulfide phase of sample
548 H4879a was not analysed because it was lost during polishing. * In sample Z1896b, the total includes 2.87
549 wt.% of tungsten that was caused by contamination from the thermocouple. †Totals include traces of Ni,
550 Co, W and Mo. *N* is the number of EPMA analysis performed on each sample.

| run | P (GPa) | T (K) | *N* | O | std | Fe | std | S | std | Cr | std | Total | std |
|---|---|---|---|---|---|---|---|---|---|---|---|---|---|
| Z1896a | 16 | 2473 | 25 | 1.14 | 0.34 | 59.67 | 0.20 | 37.45 | 0.36 | 0.15 | 0.02 | 98.48 | 0.41 |
| Z1896b* | 16 | 2473 | 26 | 0.63 | 0.22 | 60.45 | 0.31 | 34.51 | 0.23 | 0.25 | 0.02 | 98.71 | 0.35 |
| Z1913a | 18 | 2473 | 24 | 1.50 | 0.62 | 56.90 | 1.28 | 39.49 | 1.11 | 0.18 | 0.01 | 98.09 | 0.61 |
| Z1913b | 18 | 2473 | 24 | 1.18 | 0.31 | 58.82 | 0.17 | 38.09 | 0.34 | 0.24 | 0.02 | 98.34 | 0.31 |
| Z1914a | 21 | 2473 | 19 | 1.66 | 0.44 | 54.99 | 1.47 | 42.53 | 1.38 | 0.19 | 0.02 | 99.37 | 1.12 |
| Z1914b | 21 | 2473 | 20 | 1.79 | 0.25 | 57.20 | 0.97 | 40.71 | 0.94 | 0.12 | 0.01 | 99.82 | 0.27 |
| H4879a | 11 | 2473 | n.a. | n.a | n.a | n.a | n.a. | n.a. | n.a. | n.a. | n.a. | n.a. | n.a. |
| H4879b | 11 | 2473 | 20 | 2.38 | 0.53 | 57.84 | 0.44 | 38.85 | 0.38 | 0.24 | 0.01 | 99.31 | 0.68 |
| H4894 | 23 | 2473 | 17 | 1.50 | 0.25 | 57.70 | 0.77 | 38.80 | 0.84 | 0.11 | 0.01 | 98.13 | 0.34 |
| Z1930a | 8 | 2173 | 15 | 2.99 | 1.05 | 59.13 | 0.40 | 35.62 | 0.98 | 0.39 | 0.26 | 98.14 | 0.48 |
| Z1930b | 8 | 2173 | 18 | 2.61 | 0.89 | 59.52 | 0.72 | 35.88 | 0.96 | 0.40 | 0.12 | 98.42 | 0.64 |
| Z1983a | 8 | 2173 | 20 | 4.77 | 1.50 | 60.34 | 0.52 | 35.26 | 0.76 | 0.25 | 0.09 | 100.61 | 1.33 |
| Z1983b | 8 | 2173 | 21 | 5.03 | 1.03 | 59.89 | 0.43 | 35.73 | 0.71 | 0.22 | 0.03 | 100.86 | 0.64 |
| Z1987a | 8 | 2473 | 20 | 3.64 | 1.12 | 58.90 | 0.58 | 37.07 | 0.60 | 0.16 | 0.02 | 99.77 | 0.67 |
| Z1987b | 8 | 2473 | 23 | 3.05 | 1.27 | 58.38 | 0.55 | 38.05 | 0.97 | 0.18 | 0.02 | 99.66 | 0.87 |
| Z1996a | 8 | 2273 | 24 | 1.42 | 0.40 | 60.52 | 0.31 | 37.42 | 0.47 | 0.26 | 0.03 | 99.62 | 0.37 |
| Z1996b | 8 | 2273 | 22 | 1.95 | 0.87 | 60.20 | 0.39 | 37.68 | 1.25 | 0.18 | 0.03 | 100.01 | 0.54 |
| Z1640b† | 11 | 2373 | 24 | 2.22 | 0.29 | 58.06 | 0.22 | 37.51 | 0.26 | 0.12 | 0.02 | 98.76 | 0.15 |
| Z1641a† | 11 | 2273 | 45 | 2.44 | 0.13 | 56.96 | 0.15 | 37.15 | 0.32 | 0.16 | 0.02 | 98.83 | 0.23 |

This is the peer-reviewed, final accepted version for American Mineralogist, published by the Mineralogical Society of America.
The published version is subject to change. Cite as Authors (Year) Title. American Mineralogist, in press.
DOI: https://doi.org/10.2138/am-2021-7649. http://www.minsocam.org/

| | | | | | | | | | | | | | |
|---|---|---|---|---|---|---|---|---|---|---|---|---|---|
| Z1641b† | 11 | 2273 | 45 | 2.23 | 0.20 | 58.16 | 0.20 | 36.96 | 0.14 | 0.21 | 0.02 | 98.43 | 0.09 |
| H4486a† | 11 | 2473 | 45 | 1.85 | 0.11 | 56.58 | 0.21 | 38.03 | 0.24 | 0.15 | 0.01 | 98.81 | 0.10 |
| H4486b† | 11 | 2473 | 53 | 2.13 | 0.12 | 57.84 | 0.12 | 37.93 | 0.17 | 0.14 | 0.00 | 98.94 | 0.16 |
| Z1644a† | 7 | 2473 | 39 | 2.18 | 0.29 | 56.50 | 0.18 | 37.65 | 0.44 | 0.13 | 0.01 | 98.89 | 0.23 |
| Z1651a | 11 | 2623 | 35 | 1.70 | 0.02 | 56.07 | 0.20 | 38.71 | 0.08 | 0.17 | 0.00 | 99.15 | 0.17 |
| Z1651b | 11 | 2623 | 25 | 1.81 | 0.13 | 57.55 | 0.11 | 38.86 | 0.07 | 0.15 | 0.01 | 99.01 | 0.25 |

**Table 4**: Results of our multivariable regression of equations 11 and 12 for models 1 and 2 respectively using our dataset together with literature data (see text for more precision). We compare in the last columns the regression from Smythe et al. (2017).

| | **Coefficients model 1** | **Standard error** | **Coefficients model 2** | **Standard error** | **Coefficients from Smythe** | **Std error from Smythe** |
|---|---|---|---|---|---|---|
| a’ | 27 | 6 | 7.95 | 0.2 | 9.087 | 0.25 |
| b | -4621 | 368 | 18 159 | 9 536 | - | |
| c | -193 | 17 | -190 | 15 | -269 | 24 |
| $A_{Si}$ | -25 | 6 | -32 677 | 9 506 | -27 561 | 500 |
| $A_{Ti}$ | -13 | 6 | -15 014 | 9 840 | -11 220 | 1424 |
| $A_{Al}$ | -18 | 6 | -23 071 | 9 512 | -18 450 | 794 |
| $A_{Mg}$ | -16 | 6 | -18 258 | 9 634 | -13 970 | 627 |
| $A_{Fe}$ | -32 | 6 | -41 706 | 9 359 | -34 274 | 2376 |
| $A_{Ca}$ | -14 | 6 | -14 668 | 9 813 | -7 831 | 856 |
| $A_{Na}$ | -17 | 6 | -19 529 | 10 037 | -13 247 | 1414 |
| $A_{K}$ | -27 | 6 | -34 641 | 10 664 | -29 015 | 2962 |

This is the peer-reviewed, final accepted version for American Mineralogist, published by the Mineralogical Society of America.
The published version is subject to change. Cite as Authors (Year) Title. American Mineralogist, in press.
DOI: https://doi.org/10.2138/am-2021-7649. http://www.minsocam.org/

| | | | | | | |
|---|---|---|---|---|---|---|
| $A_H$ | -19 | 6 | -22 677 | 9 674 | -17 495 | 561 |
| $A_{SiFe}$ | 76 | 4 | 120 662 | 7 048 | 116 568 | 6066 |

555

556 **Figures**

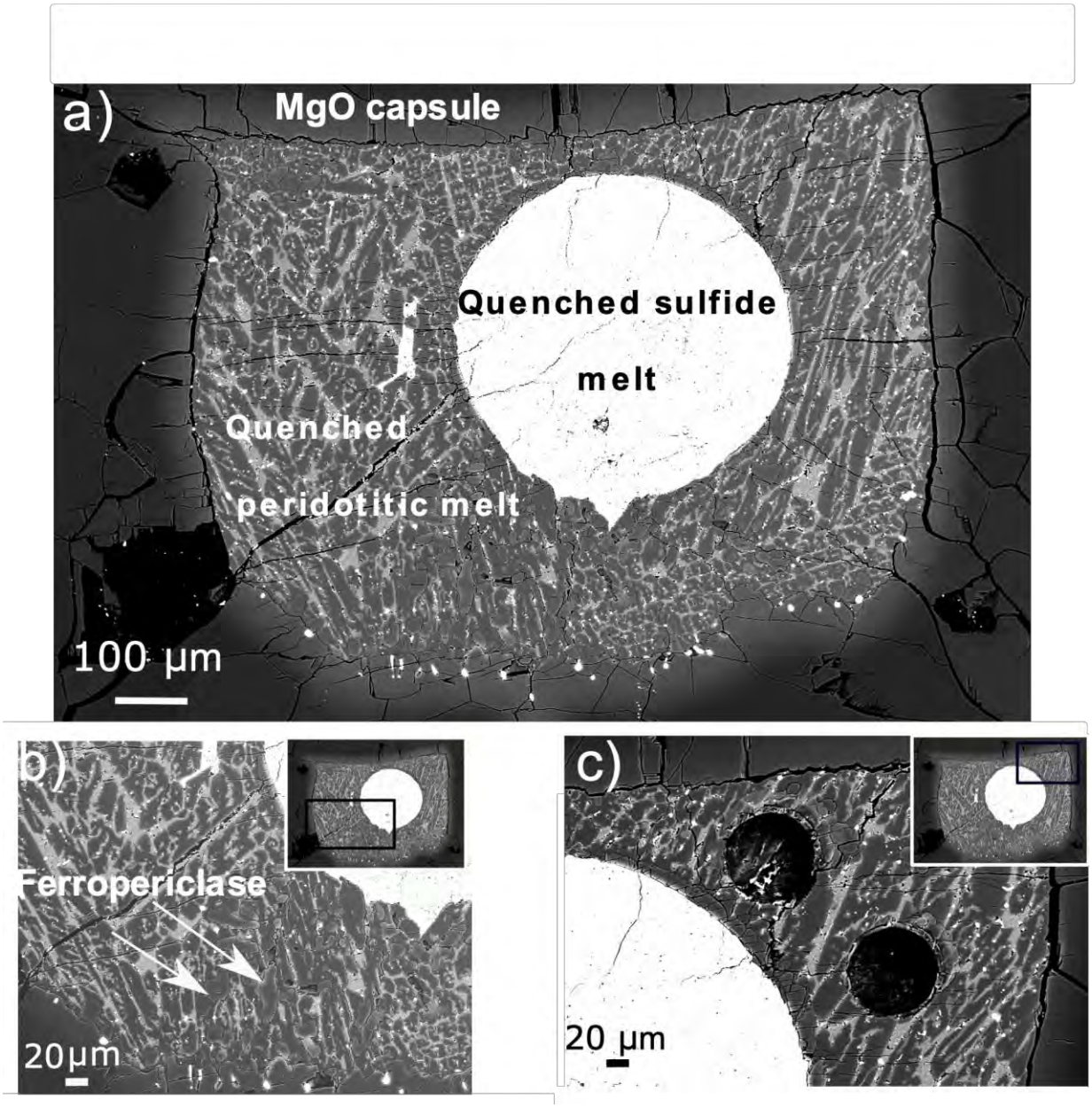


557

558 Figure 2

559

This is the peer-reviewed, final accepted version for American Mineralogist, published by the Mineralogical Society of America.
The published version is subject to change. Cite as Authors (Year) Title. American Mineralogist, in press.
DOI: https://doi.org/10.2138/am-2021-7649. http://www.minsocam.org/

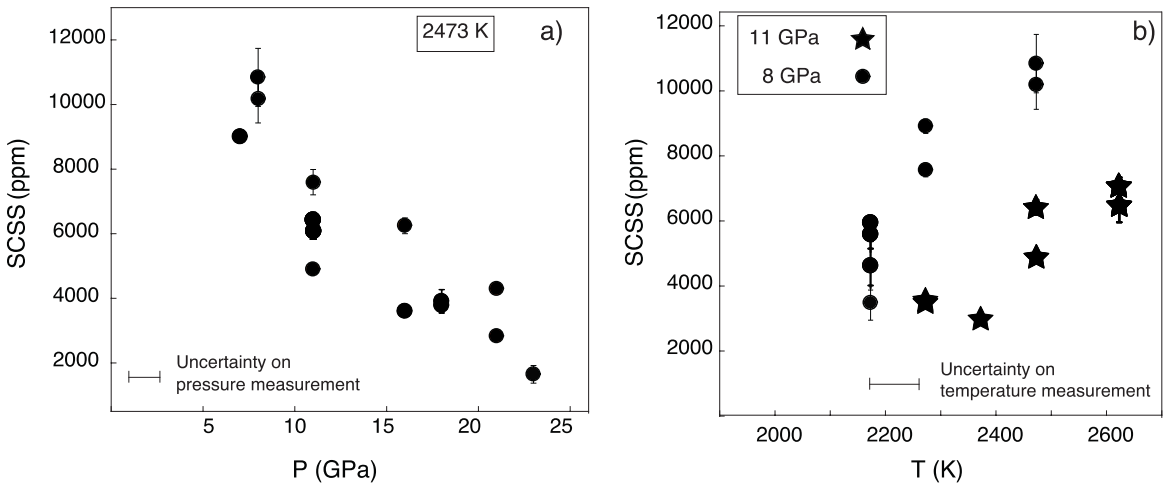


560

561 Figure 2

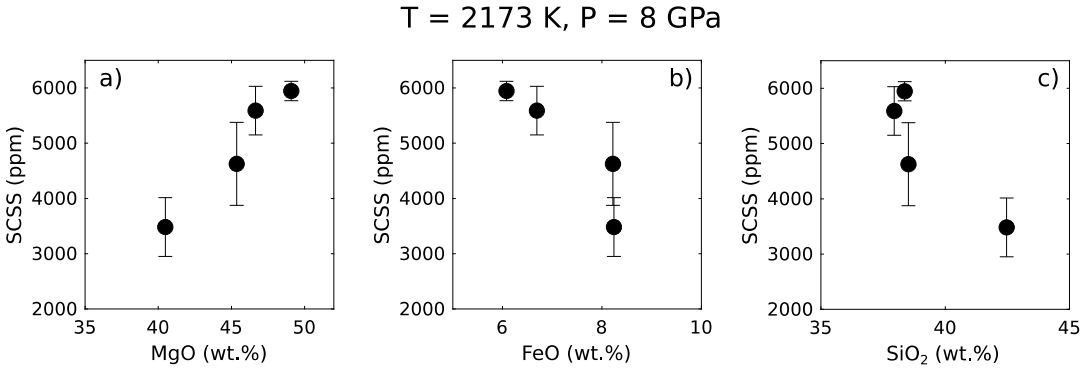


562

563

564 Figure 3

This is the peer-reviewed, final accepted version for American Mineralogist, published by the Mineralogical Society of America.
The published version is subject to change. Cite as Authors (Year) Title. American Mineralogist, in press.
DOI: https://doi.org/10.2138/am-2021-7649. http://www.minsocam.org/

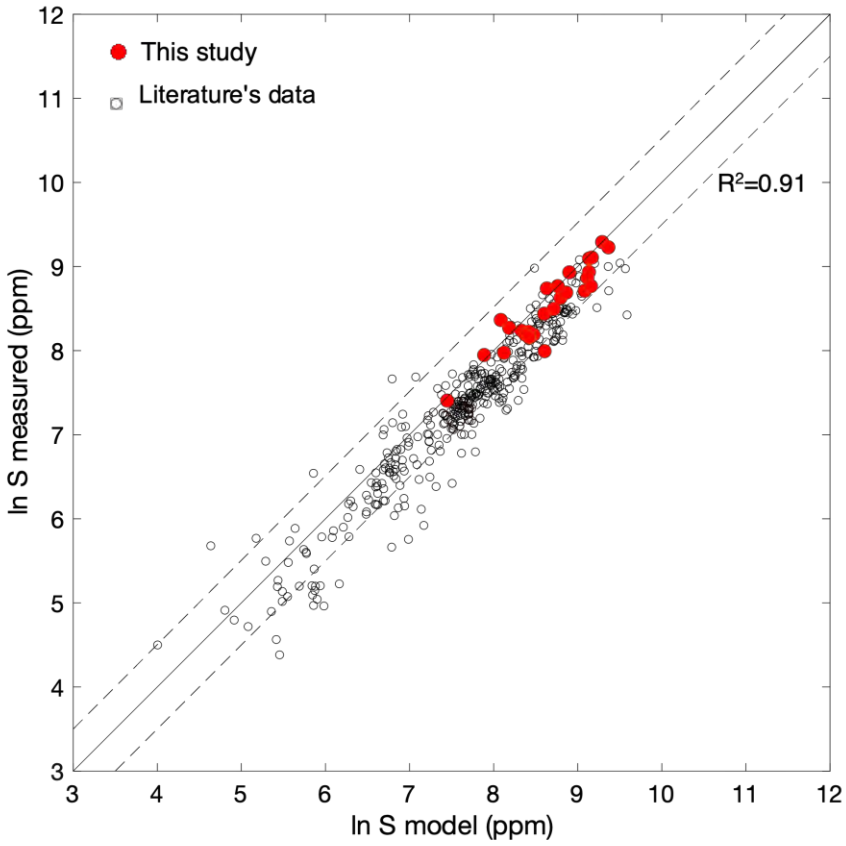


565

566 Figure 4

This is the peer-reviewed, final accepted version for American Mineralogist, published by the Mineralogical Society of America.
The published version is subject to change. Cite as Authors (Year) Title. American Mineralogist, in press.
DOI: https://doi.org/10.2138/am-2021-7649. http://www.minsocam.org/

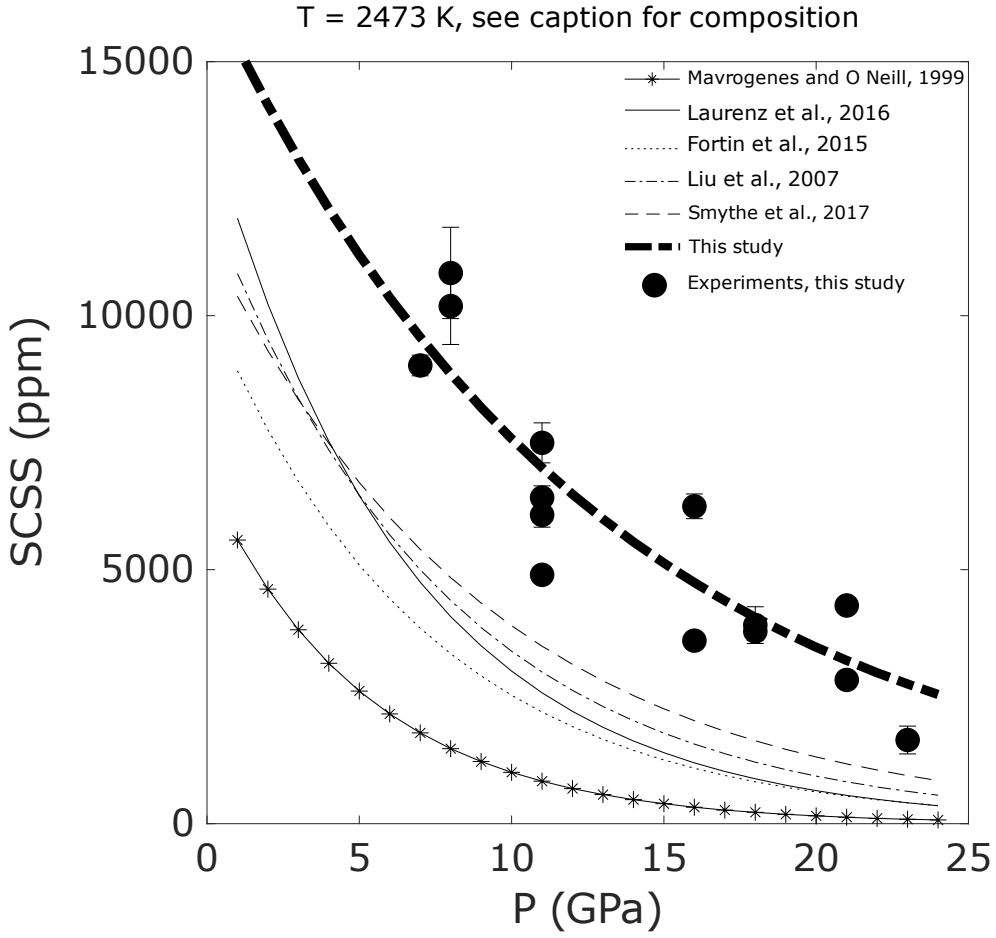


Figure 5

This is the peer-reviewed, final accepted version for American Mineralogist, published by the Mineralogical Society of America.
The published version is subject to change. Cite as Authors (Year) Title. American Mineralogist, in press.
DOI: https://doi.org/10.2138/am-2021-7649. http://www.minsocam.org/

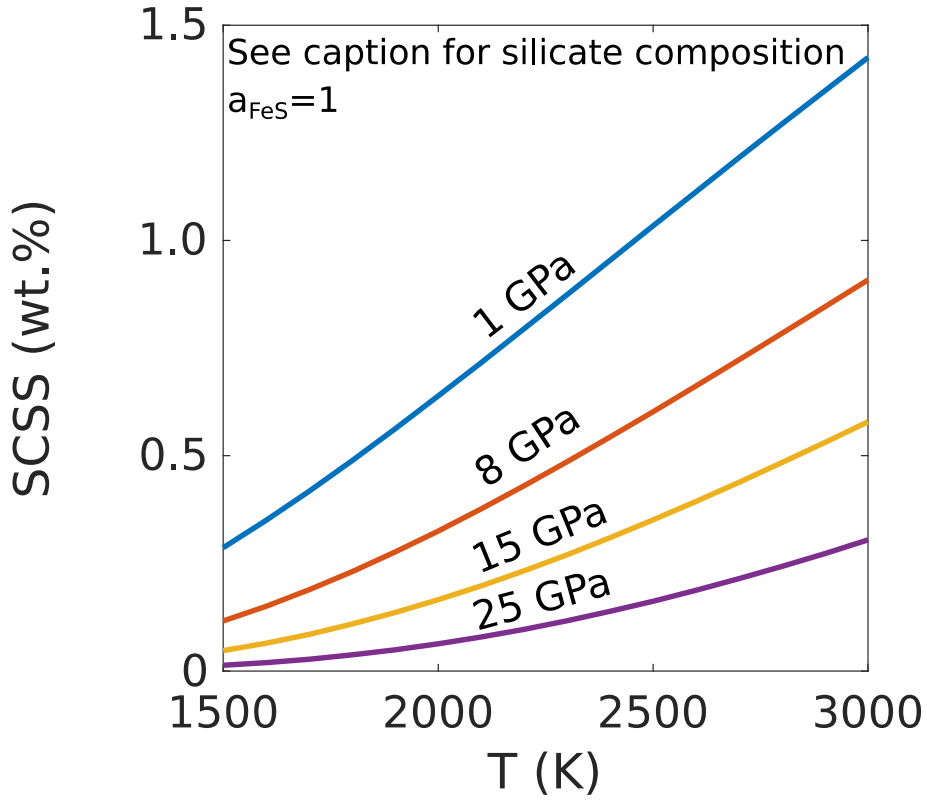


571

572 Figure 6:

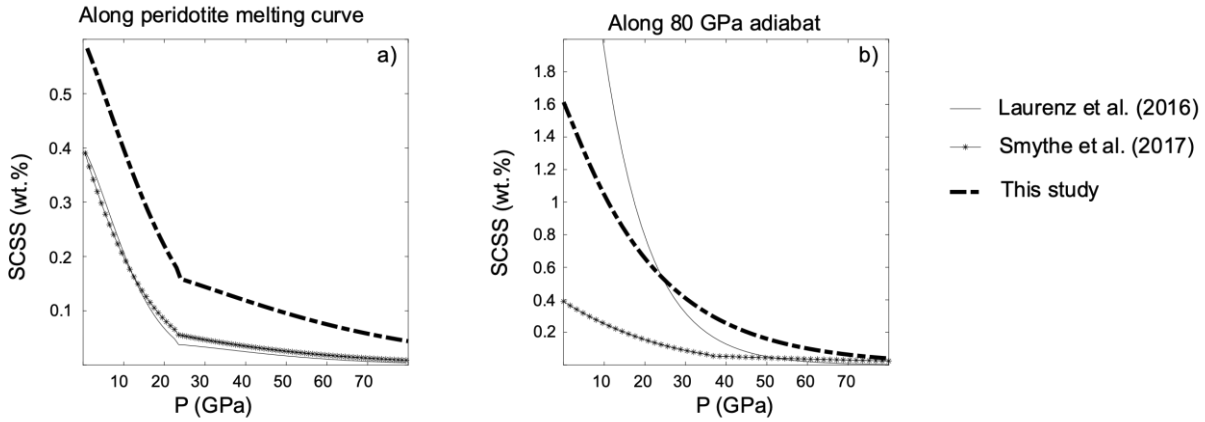


573

574 Figure 7:

575

This is the peer-reviewed, final accepted version for American Mineralogist, published by the Mineralogical Society of America.
The published version is subject to change. Cite as Authors (Year) Title. American Mineralogist, in press.
DOI: https://doi.org/10.2138/am-2021-7649. http://www.minsocam.org/

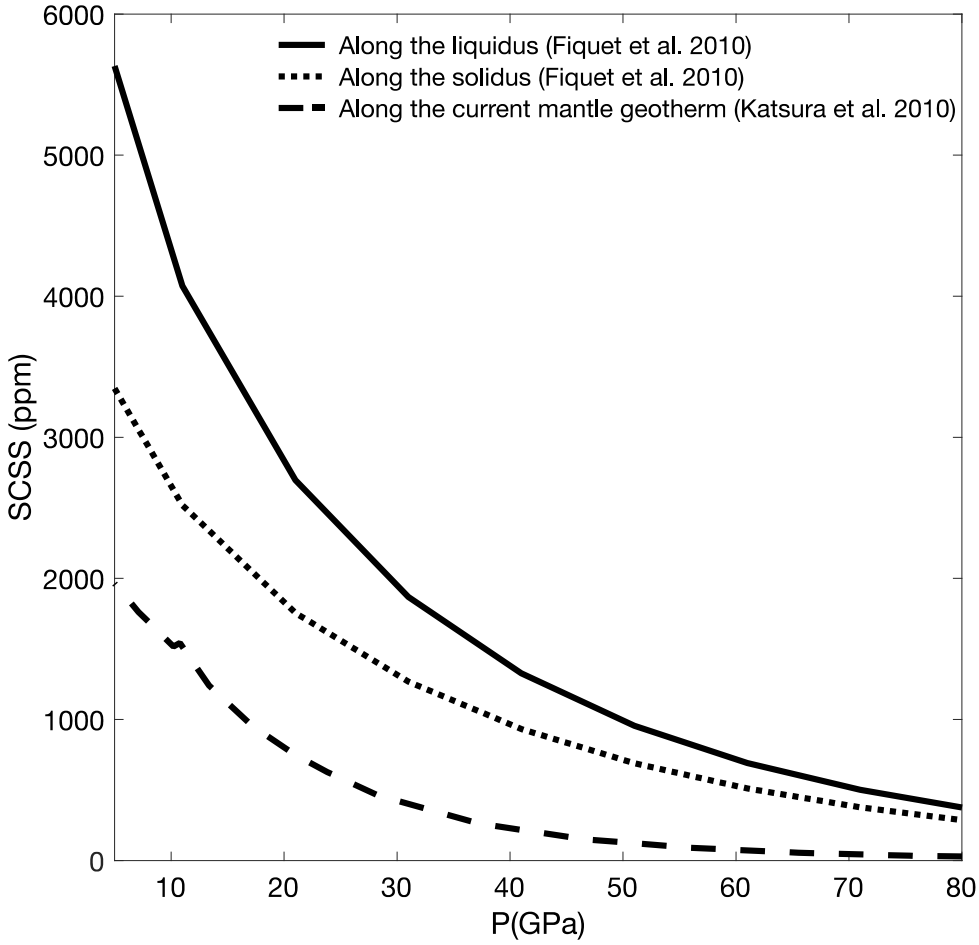


576

577 Figure 8:

578